

## Drop Size Ambiguities in the Retrieval of Precipitation Profiles from Dual-Frequency Radar Measurements

ZIAD S. HADDAD, JONATHAN P. MEAGHER, AND STEPHEN L. DURDEN

*Jet Propulsion Laboratory, California Institute of Technology, Pasadena, California*

ERIC A. SMITH

*NASA Goddard Space Flight Center, Greenbelt, Maryland*

EASTWOOD IM

*Jet Propulsion Laboratory, California Institute of Technology, Pasadena, California*

(Manuscript received 14 November 2003, in final form 15 December 2005)

### ABSTRACT

The threat of flooding from landfalling tropical cyclones is a function of the local variation in rain rate and rain accumulation. To date, these have been inferred from single-frequency radar reflectivity measurements. However, the Tropical Rainfall Measuring Mission experience has confirmed that one of the main difficulties in retrieving rain profiles using a single-frequency radar is the unknown raindrop size distribution (DSD). A dual-frequency radar such as the one planned for the upcoming Global Precipitation Measurement (GPM) core satellite is expected to help sort out at least part of this DSD-induced ambiguity. However, the signature of precipitation at 14 GHz does not differ greatly from its signature at 35 GHz (the GPM radar frequencies). To determine the extent of the vertical variability of the DSD in tropical systems and to quantify the effectiveness of a dual-frequency radar in resolving this ambiguity, several different models of DSD shape are considered and used to estimate the rain-rate and mean-diameter profiles from the measurements made by Jet Propulsion Laboratory's (JPL's) airborne second generation precipitation radar (PR-2) over Hurricanes Gabrielle and Humberto during the Fourth Convection and Moisture Experiment (CAMEX-4) in September 2001. It turns out that the vertical structures of the rain profiles retrieved from the same measurements under different DSD assumptions are similar, but the profiles themselves are quantitatively significantly different.

### 1. Introduction

Once a tropical cyclone makes landfall, one of its main dangers is the flooding it often causes. This threat of flooding is a function of the rain rate as well as the total surface rain accumulation. The precipitation can be quite drastically affected by local orographic forcing as well as interactions with any midlatitude frontal boundaries or upper-level troughs. That is why it is very desirable to monitor the rainfall within tropical cyclones at fine temporal and spatial scales. While this can be achieved using weather radar, the measurement of surface rainfall with radar is not without problems,

chief among them being the dependence of the nonlinear relation between the measured radar reflectivities  $Z$  and the underlying rain rate  $R$  on the sizes of the raindrops. The latter can vary significantly within a tropical cyclone. In convective areas, large hydrometeors tend to precipitate out locally, while smaller ones tend to be carried aloft to be precipitated out in stratiform areas. Since the reflectivity of a raindrop is roughly proportional to the square of its mass, small errors in the a priori assumption about the drop sizes in any given column of rain can easily produce large errors in the inferred rain rate. This problem has been dealt with in two ways. A concerted effort has been made to describe the drop size distribution (DSD) in various rain regimes using in situ measurements obtained by ground-based disdrometers as well as airborne optical probes. While such data can yield statistical descriptions about rain-

---

Corresponding author address: Ziad S. Haddad, 300-243 JPL, California Institute of Technology, Pasadena, CA 91109-8099.  
E-mail: zsh@jpl.nasa.gov

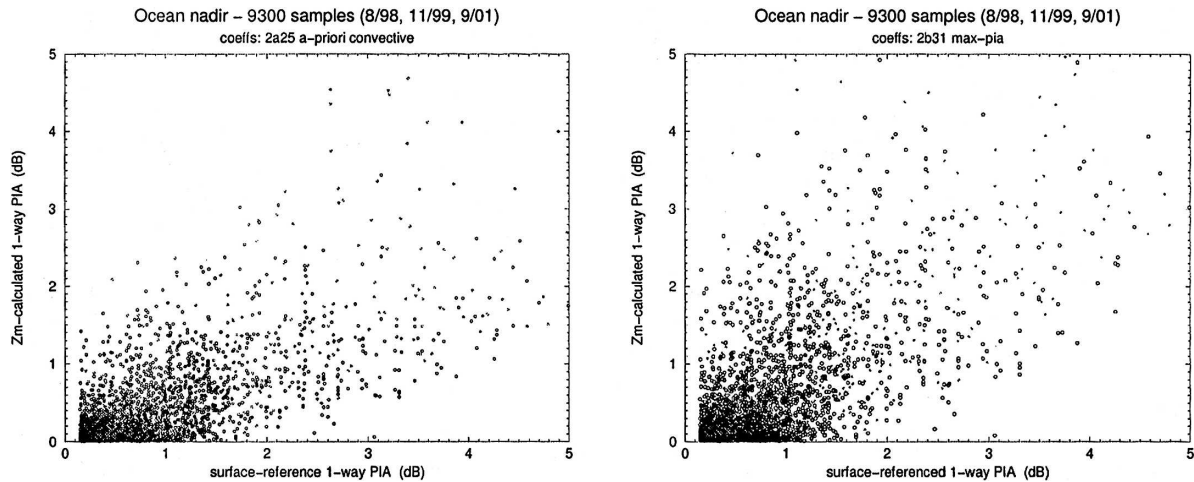


FIG. 1. The  $Z_m$ -derived PIA vs surface-reference estimates from the TRMM data, showing poor correlation at moderate and low precipitation (convective cases are shown in red, stratiform in black).

drop size variability, they are limited by the fact that the instruments involved can only sample a minuscule volume of air relative to the large volumes that are probed by even the highest resolution radars. It is therefore not at all clear how representative the statistics obtained from in situ data are of the rain in any specific precipitating column. An alternate procedure to quantify these statistics and to make them more specifically relevant to any particular area within a tropical cyclone is to design radars that can simultaneously measure both the rain rate and the underlying mean drop size. This approach requires a dual-frequency radar, with the assumption that the reflectivities measured at two different frequencies depend in an invertible way on the underlying rain rate and mean drop size. Indeed, the original proposal for the precipitation radar designed for the Tropical Rainfall Measuring Mission (TRMM) specified a Ku-band as well as a Ka-band channel. The latter was eventually dropped because of budget constraints, but the dual-frequency design is being implemented for the upcoming Global Precipitation Mission.

The rain-profiling algorithm development and validation effort undertaken for TRMM has confirmed that one of the main difficulties surrounding the retrieval of rain rate profiles from spaceborne radar reflectivity measurements is the unknown DSD. Indeed, if one starts with the assumption that the DSD is always an exponential (or, at worst, a gamma) distribution, whose dependence on the rain rate is known a priori, one can then derive power-law relations  $Z = aR^b$  and  $k = \alpha R^\beta$  which very adequately relate the 14-GHz radar reflectivity factor  $Z$  and the 14-GHz attenuation coefficient  $k$  to the rain rate  $R$ . It follows (see, e.g., Haddad et al. 1995) that the one-way path-integrated attenuation

(PIA), integrated over a vertical rain column, must be related to the 14-GHz measured reflectivities  $Z_m$  in that column by

$$\text{PIA} = \left[ 1 - 0.2 \log(10) \alpha \frac{\beta}{b} \int (Z_m/a)^{\beta/b} \right]^{b/\beta}. \quad (1)$$

Figure 1 is a plot of the PIA values obtained from the TRMM radar measurements over the ocean during several orbits by comparing the rainy surface return with the average surface return from the nearby clear-air regions. This surface-reference PIA is shown on the horizontal axis, while the vertical axis represents the right-hand side of (1) calculated with two different DSD assumptions (corresponding to a few different sets of constant  $a$ ,  $b$ ,  $\alpha$ , and  $\beta$ ). The left panel shows the result of using the a priori values of the parameters  $a$ ,  $b$ ,  $\alpha$ , and  $\beta$  in the TRMM radar algorithm (Iguchi et al. 2000); the right panel shows the result of using those parameters in the multiple DSD TRMM combined radar/radiometer algorithm (Haddad et al. 1997b), which produce the largest attenuation. If (1) were verified exactly, one would expect much less scatter than is evident in the plots. Indeed, for one-way attenuations below 1.5 dB, there does not seem to be any correlation between the two sides of (1), though there is a clear tendency for the  $Z$ -calculated values to be much smaller than the surface-referenced ones. This apparent failure of Eq. (1) could be caused in part by the change in the surface backscattering cross section due to the variation of the wind from the clear-air regions to the rainy area. But a systematic increase or decrease of the backscattering within the precipitation would result in a bias of the estimates. The fact that such a bias is not

evident in the figure leads to the conclusion that whatever systematic change in the wind between the clear and rainy areas is not sufficient to explain the large mismatch in PIAs at moderate and low precipitation. Indeed, this discrepancy constitutes compelling evidence that the DSD parameters vary very significantly over a rain column.

In the case of TRMM, this DSD problem has been dealt with in two ways. In the radar algorithm, (1) is used to adjust the ratio  $\alpha\beta/b$  and thus reduce the ambiguity, at least in the case of heavier precipitation. In the Bayesian framework of the TRMM combined radar/radiometer algorithm, (1) is used to weight the candidate a priori DSDs in favor of the better-matching ones, and the observed radiances are also used to further constrain the multiple possibilities for the DSD. The dual-frequency radar that the Global Precipitation Measurement (GPM) mission's core satellite will carry should prove a much more effective tool in sorting out at least part of this DSD-induced ambiguity. Indeed, with two radar reflectivity profiles, one would expect to be able to retrieve not just a single rain-rate profile, but in addition at least one first-order DSD profile, for example, a profile of the (mass weighted) mean drop diameter  $D^*$ . Unfortunately, this expectation may turn out to be difficult to fulfill, because the reflectivity profiles at the two radar frequencies are far from independent. After all, lighter rain is made up mostly of small drops. As Fig. 2 shows, the backscattering cross section of small drops is not significantly different at 14 and 35 GHz. One would therefore not expect large differences in the associated radar reflectivity factors. While the difference in the extinction cross section appears more readily exploitable for small drops, its actual magnitude is unfortunately so small that the resulting attenuation is not significant for light precipitation. At the other extreme, while the attenuation will be appreciable (at both frequencies) for heavy rain, it is in fact likely to be so appreciable as to drive the backscattered 35-GHz signal itself below the sensitivity threshold of that channel. Thus, the two frequencies are not very different at low rain rates, and they will in effect reduce to a single frequency at high rain rates, leaving a somewhat disappointing range over which the two frequencies can be realistically expected to resolve the DSD-induced ambiguity problem. That is why it is at least as important for GPM as it was for TRMM to develop an optimal approach to extract from all the GPM core satellite's measurement profiles of the best unbiased estimates of the means of the rain rate  $R$  and mass-weighted mean diameter  $D^*$ . The purpose of this paper is to quantify the effect of different plausible a priori assumptions about the possible shapes of the DSD on the retrieved

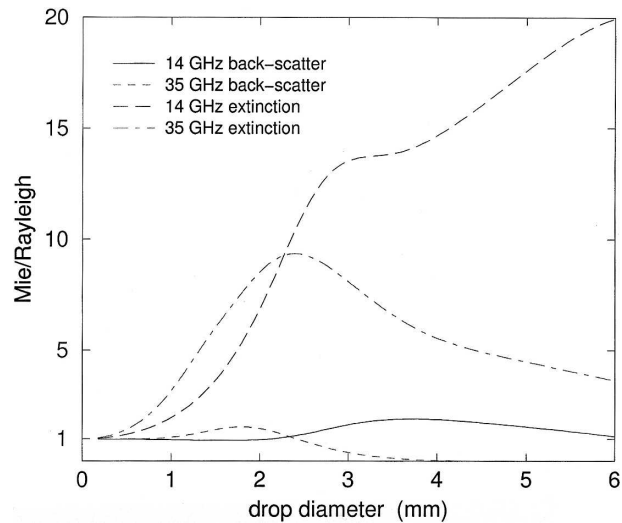


FIG. 2. Actual (Mie) vs small-size-approximation (Rayleigh) microwave signatures of raindrops.

precipitation profiles using tropical cyclone data from the Fourth Convection and Moisture Experiment (CAMEX-4).

The aim of this work is not to propose a specific retrieval methodology. Many dual-frequency rain-profiling algorithms have been proposed to date, starting with those developed by Eccles and Mueller (1971), Fujita (1983), Meneghini and Nakamura (1990), and Marzoug and Amayenc (1994). These approaches start by making some simplifying assumptions to reduce the DSD description to an analytic form using two parameters, and proceed to prescribe a procedure to retrieve the latter given a pair of reflectivity profiles at two frequencies. Our goal is to assess the effect of a priori DSD assumptions, including the possibility of considering DSDs that are not given by any analytic form but rather coming directly from extensive collections of in situ measurements. That is why we tried to avoid any specific deterministic retrieval algorithms, and relied instead on obtaining Bayesian estimates of the (conditional) mean rain rate and mass-weighted mean drop diameter, given the measured reflectivities and given each a priori model of the allowed DSD shapes. The models considered are listed in section 2, and the Bayesian estimation is discussed in section 3. The results for the CAMEX-4 data are described in section 4.

## 2. Different DSD models

We shall consider five well-documented liquid DSD models. No discussion of DSDs can be complete without considering Marshall and Palmer's exponential form (Marshall and Palmer 1948)

$$N_{MP}(D) = N_0 e^{-\Lambda D}, \quad (2)$$

in which, if we assume a nominal terminal fall velocity of  $9.56(1 - e^{-0.53D})$  m s<sup>-1</sup> for drops of diameter  $D$  mm, the parameters  $N_0$  and  $\Lambda$  must be consistent with  $R$ , that is, must satisfy

$$R = 0.11 \left[ \frac{1}{\Lambda^4} - \frac{1}{(\Lambda + 0.53)^4} \right] N_0 \text{ mm h}^{-1}, \quad (3)$$

with  $N_0$  in mm<sup>-1</sup> m<sup>-3</sup>. Thus, in addition to  $R$ , the exponential  $N_{MP}$  has a single parameter. As long as Eq. (3) is enforced, whether one chooses to identify this parameter as  $N_0$  or  $\Lambda$  makes no difference whatsoever, and we shall choose  $\Lambda$ , with the additional constraint that the ratio  $4/\Lambda$ , which is equal to the mass-weighted mean drop diameter, not exceed 3 mm. The second, third, and fourth DSD models that we consider are special cases of the gamma DSD

$$N_{\Gamma}(D) = N_0 D^{\mu} e^{-\Lambda D}. \quad (4)$$

This distribution effectively depends on two parameters in addition to  $R$ . There are several ways of constraining one of these parameters to end up with only two unknowns that can be solved for using the two measured radar reflectivity factors. One that has proved consistent with disdrometer and airborne 2D-probe (small) sample statistics consists of reexpressing  $\mu$  and  $\Lambda$  in terms of the mass-weighted mean drop diameter  $D^*$  and the dimensionless relative mass-weighted rms diameter deviation  $s^*$ , and enforcing on the pair  $(D^*, s^*)$  the rather restrictive joint behavior quantified by the sample statistics observed during the Tropical Ocean Global Atmosphere Coupled Ocean–Atmosphere Response Experiment (TOGA COARE) campaign (Lukas et al. 1995) and during the 1992–93 Darwin field measurements (Haddad et al. 1997a). Roughly, these restrictions amount to requiring that  $D^* R^{-0.155}$  have a mean of about 1.1 (with  $R$  in mm h<sup>-1</sup> and  $D^*$  in mm) and a standard deviation of about 0.3, while  $s^* D^*{}^{-0.165} R^{-0.011}$ , which has a mean of about 0.4 and a tiny standard deviation smaller than 0.05, is fixed at 0.4 so that  $D'' = D^* R^{-0.155}$  is the independent DSD parameters in this case. We shall refer to the resulting restricted gamma DSD model as  $N_{\Gamma_0}$ . This is the second DSD that we shall consider. It is the one used in the TRMM combined radar/radiometer algorithm. The third and fourth DSD models are similar restrictions of the gamma model, obtained from (4) by imposing a deterministic relation between  $N_0$  and  $\mu$ . We chose the relation (Ulbrich and Atlas 1998)

$$N_0 = 6734 e^{1.45\mu} \text{ mm}^{-1-\mu} \text{ m}^{-3} \quad (5)$$

for the third model  $N_{\Gamma_1}$ , and the relation (Ulbrich 1983)

$$N_0 = 1500 e^{0.84\mu} \text{ mm}^{-1-\mu} \text{ m}^{-3} \quad (6)$$

for the fourth model  $N_{\Gamma_2}$ . Finally, we also consider a model that does not depend on any closed analytic form for the distribution function  $N$ . After all, there is an enormous wealth of sampled DSDs measured from various probes, and there is no reason not to use a large subgroup of such samples as an a priori database in lieu of a model. Indeed, for our fifth DSD model  $N_C$ , we chose the TOGA COARE database of DSD samples collected by the National Center for Atmospheric Research (NCAR) 2-D Particle Measuring System (PMS) probes mounted on the NCAR Electra aircraft over the warm pool of the western equatorial Pacific between November 1992 and February 1993. A principal component analysis (Meagher and Haddad 2002) had reduced this dataset and produced a more efficient way to code the data. But the resulting savings in computer resources (memory and processing) are not significant for the current study and we used the original database of DSD samples itself.

The next step is to calculate the Mie extinction and backscattering efficiencies as a function of drop diameter. Once this is done, one can associate to each rain rate/DSD pair  $(R, N)$  in any one of our five models the corresponding radar reflectivity factors  $z_{14}(R, N)$  and  $z_{35}(R, N)$  (in mm<sup>6</sup> m<sup>-3</sup>), and the corresponding attenuation coefficients  $k_{14}(R, N)$  and  $k_{35}(R, N)$  (in dB km<sup>-1</sup>). Figure 3 shows the resulting reflectivity manifolds [to borrow a term dear to the passive radiometer community, see, e.g., Smith and Mugnai (1988)] for each of our DSD models. In the case of  $N_{MP}$ ,  $N_{\Gamma_0}$ ,  $N_{\Gamma_1}$ , and  $N_{\Gamma_2}$ , these manifolds were obtained by choosing a few representative values for the free DSD parameter ( $\Lambda$  in the case of  $N_{MP}$ ,  $N_{\Gamma_1}$ , and  $N_{\Gamma_2}$ ,  $D''$  in the case of  $N_{\Gamma_0}$ ), and letting  $R$  vary from 0.2 to 200 mm h<sup>-1</sup>. In the case of  $N_C$ , the manifold is computed directly from the DSD samples in the database. In all cases, the value of the difference  $z_{14}(R, N) - z_{35}(R, N)$  is plotted versus  $z_{14}(R, N)$ . The first observation is that, for all five DSD models, when the 14-GHz reflectivities are small, the rain-rate curves are almost horizontal, confirming our previous observation that for lighter precipitation there is no significant difference between the two frequencies.

There are two additional facts illustrated by the figure that are crucial to the retrieval problem. The first is that all the curve crossings correspond to retrieval ambiguities: they indicate that a pair of (14-GHz, 35-GHz) reflectivity factors can be explained by at least two rain rates (which can differ by a factor of 2 or more, the

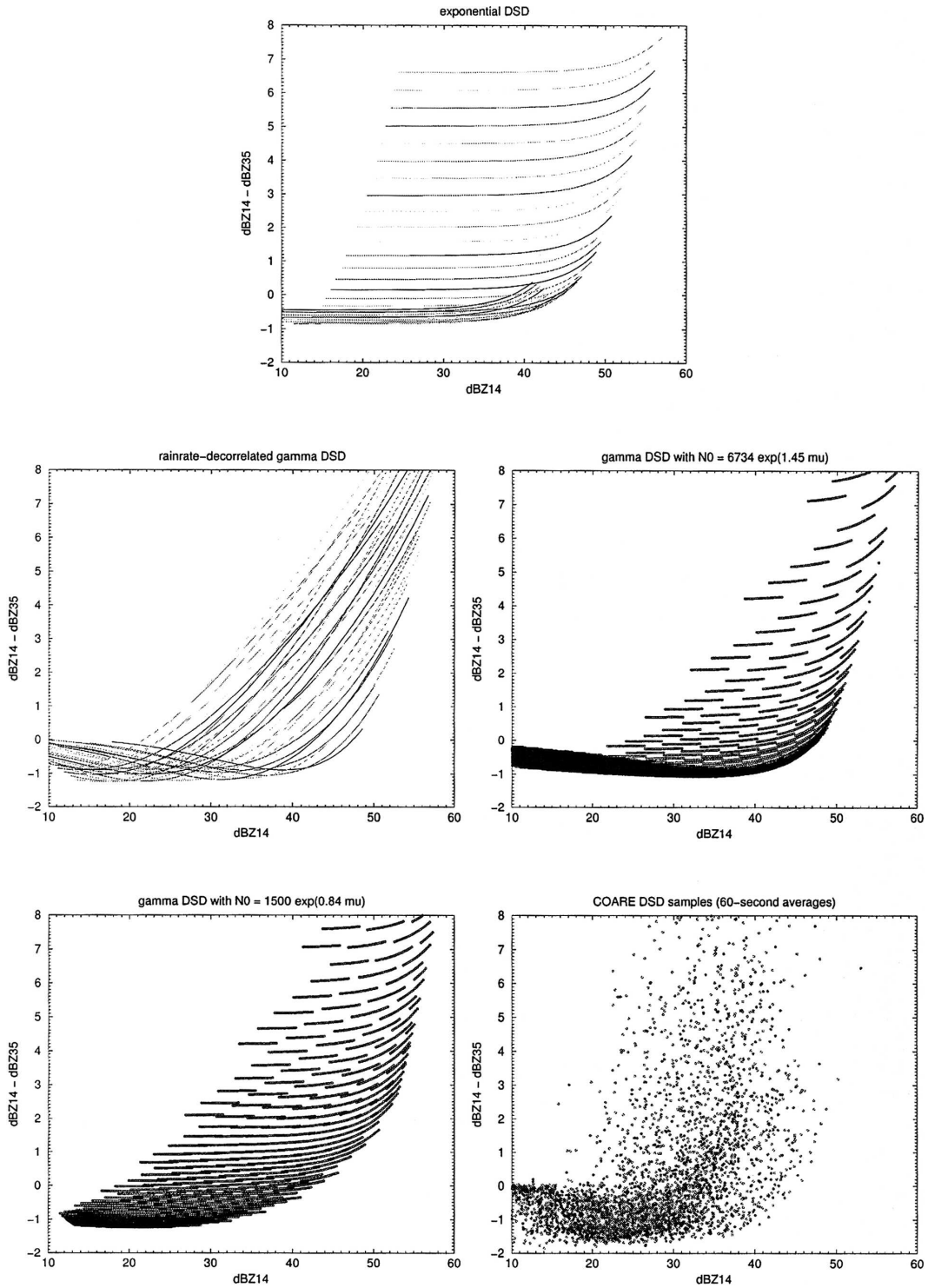


FIG. 3. Reflectivity manifolds ( $z_{14} - z_{35}$ ) vs  $z_{14}$  for the DSDs (top)  $N_{MP}$ , (middle left)  $N_{\Gamma_0}$ , (middle right)  $N_{\Gamma_1}$ , (lower left)  $N_{\Gamma_2}$ , and (lower right)  $N_C$ , showing the flow lines for the rain rate  $R$  in the first two cases (each curve corresponds to a fixed value of the free parameter of the respective DSD, namely  $N_0$  in the case of  $N_{MP}$ , and  $D'' = D * R^{-0.155}$  in the case of  $N_{\Gamma_0}$ ), and showing one point for typical values of  $(R, \mu, \Lambda)$  considered in the case of  $N_{\Gamma_1}$  and  $N_{\Gamma_2}$ , showing all the DSD sampled during the TOGA COARE campaign in the case of  $N_C$ .

two-dimensional manifolds could not be readily made to illustrate this ambiguity quantitatively), associated to different DSD parameter values. This implies that even in the absence of any observation noise, the dual-frequency retrieval problem can be ambiguous, and manifestly more so in the case of  $N_{MP}$  than in the other cases, though all the models have nonnegligible ambiguities at low precipitation. Since these ambiguities are intrinsic to the dual-frequency observations, one would need to consider additional measurements to resolve them. The second point concerns the blank regions in the plots. These are most evident in the least ambiguous cases  $N_{R_0}$  and  $N_{R_1}$ , though they are not entirely absent in the other models. Indeed, current technology cannot guarantee that the noise in the reflectivity measurements is less than about 0.3 dB rms at best. Thus, one's actual observations could quite easily fall outside the region covered by our manifolds, that is, it is quite likely that with any DSD model one will face the situation where no rain rate can explain exactly a pair of (noisy) reflectivities. Therefore, when attempting a retrieval, one must have a rigorous mechanism to assess the plausibility of the various model pairs that are close to the measured pair. In summary, a dual-frequency radar cannot entirely avoid the ambiguities with which we have been all too familiar in the case of the TRMM radar, and the noise in the measurements (along with the unavoidable imperfection of any DSD model) will make it essential to allow for multiple inexact matches. Both of these concerns make it highly desirable to use a Bayesian framework to make unbiased estimates of the precipitation underlying the measurements.

There is yet another problem which leads us to consider a sixth case. It is brought about by the need to account for the cumulative attenuation at both frequencies as one estimates the rain rate sequentially through the consecutive vertical range bins in the cloud. It is however easiest to describe this sixth case once the retrieval approach has been outlined in the following section.

### 3. Dual-frequency Bayesian retrieval

To keep the problems associated with the specific retrieval procedure separate from the DSD ambiguities themselves, we applied the simplest Bayesian approach to the dual-frequency profiling problem. Let us start by fixing the notation. For a given vertical column of precipitation, call  $Z_{14}(i)$  [ $Z_{35}(i)$ , respectively] the radar reflectivity factor measured from the  $i$ th vertical range bin at 14 (35) GHz, with  $i = 1$  for the first bin at the top of the rainy cloud and increasing downward. The equations that have to be solved for the rain rate/DSD pair  $(R, N)$  at each range bin  $i$  are

$$Z_{14}(i) = z_{14}(R, N) - 2A_{14}(i - 1) + \text{noise}_{14} \quad \text{and} \quad (7)$$

$$Z_{35}(i) = z_{35}(R, N) - 2A_{35}(i - 1) + \text{noise}_{35}, \quad (8)$$

where  $A_{14}(i - 1)$  [ $A_{35}(i - 1)$ ] is the one-way 14- (35-) GHz attenuation accumulated from the top of the cloud until the  $i$ th range bin, expressed in dB. To solve Eqs. (7)–(8) for the unknowns  $R$  and  $N$ , one would thus need to track the accumulated attenuations  $A_{14}$  and  $A_{35}$ . Assuming that the noise terms  $\text{noise}_{14}$  and  $\text{noise}_{35}$  are zero-mean Gaussian with variances  $\sigma_{14}^2$  and  $\sigma_{35}^2$ , the simplest Bayesian approach consists of two steps repeated recursively for the consecutive range bins:

- 1) Starting at the top of the cloud ( $i = 1$ ), and setting  $A_{14}(0) = A_{35}(0) = 0$ , consider all realistic rain rates  $R$  and all DSDs  $N$  allowed by the a priori model, and calculate for each pair  $(R, N)$  its mean-squared distance  $d_i$  from the two independent measurements:

$$d_i(R, N) = \left\{ \frac{[Z_{14}(i) + 2A_{14}(i - 1)] - z_{14}(R, N)}{\sigma_{14}} \right\}^2 + \left\{ \frac{[Z_{35}(i) + 2A_{35}(i - 1)] - z_{35}(R, N)}{\sigma_{35}} \right\}^2. \quad (9)$$

The optimal unbiased estimate of the rain rate would then have to be given by

$$\hat{R}(i) = \sum_N \int R p_i(R, N) dR, \quad (10)$$

where  $p_i$  is the probability weight  $p_i(R, N) = e^{-0.5d_i(R, N)}$ , normalized so that  $\sum p_i = 1$ .

- 2) The corresponding accumulated attenuation up to and including the current range bin must then be updated, using the similar formula

$$A_f(i) = A_f(i - 1) + \sum_N \int \delta k_f(R, N) p_i(R, N) dR, \quad (11)$$

where  $\delta$  is the thickness of the range bin (in km), and  $f = 14$  or 35 GHz. This is the Bayesian retrieval approach that we used.

Before illustrating this method and comparing its retrievals with the five a priori DSD cases, we shall now describe a sixth case, which we had to consider for completeness. It comes about because Eqs. (7)–(8) are not exactly correct. Indeed, rain is not the only source of attenuation of microwaves in the atmosphere. While absorption by oxygen and water vapor is relatively small and largely predictable, the attenuation due to cloud liquid water, especially at 35 GHz, is not negli-

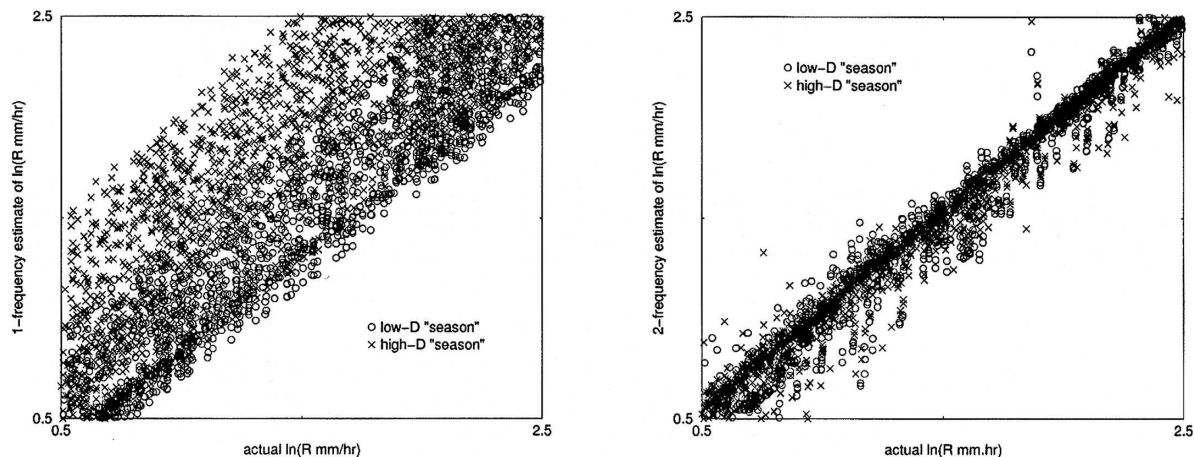


FIG. 4. Estimated vs original rain rates, with small-drop cases indicated with  $\times$  and the large-drop cases indicated with  $\circ$ . (left) The single-frequency retrievals, which misinterpret the changing DSD, resulting in biased estimates, and (right) the dual-frequency Bayesian estimates.

gible. That is because the downward-looking radar will measure

$$Z(i) = \int \int \int \left[ \int_{(i-1)\delta}^{i\delta} z(r, \theta, \phi) e^{-\int_r^{\text{top}} k(r', \theta, \phi) dr'} dr \right] d\theta d\phi, \quad (12)$$

and while  $z$  in the right-hand side is the radar reflectivity factor of the rain, the attenuation coefficient  $k$  is the sum  $k_{\text{rain}} + k_{\text{cloud}}$  of the attenuations due to the precipitation and to the cloud (the reflectivity of the cloud droplets is negligible because it is proportional to the sixth power of the droplet diameter). At 35 GHz, if  $M$  is the cloud liquid water content in  $\text{g m}^{-3}$ ,  $k_{\text{cloud}} \approx \kappa M \text{ dB km}^{-1}$ , with  $\kappa = 0.84 \text{ m}^3 \text{ g}^{-1} \text{ dB km}^{-1}$  when all cloud droplets are  $10 \mu\text{m}$  in diameter (and  $\kappa$  increases toward a value of 1.4 when all drops approach drizzle size). Thus, while the cloud is not sufficiently reflective to be detectable, it will cast a shadow, and this shadow may differ in clear air and within the rain. For example, a rather moderate two vertical kilometers of liquid cloud carrying  $0.5 \text{ g m}^{-3}$  of water will attenuate the 35-GHz signal by about 1 dB. This presents two problems. First, the surface cross section in clear air (i.e., where the reflectivities from the atmosphere do not exceed the relatively high radar noise threshold), which is necessary to the proper estimation of the integrated attenuation within precipitation, would be underestimated if no account is taken of the attenuation due to any undetected cloud. This would result in an underestimate of the PIA, and that is the main reason we chose not to use any a priori information about the PIA in our retrieval approach. Second, within the precipitation, at each vertical resolution bin one must estimate (and re-

move) the attenuation in the left-hand side of (12), and this cannot be done without biasing the estimate if one does not know how to apportion the attenuation between precipitating and nonprecipitating liquid. We decided to test the effect of this cloud shadow problem by considering a sixth case, where the DSD is the TOGA COARE database of  $N_C$ 's as in the fifth DSD model, but where we systematically assume the existence of cloud liquid with liquid water content  $M$  ( $\text{g m}^{-3}$ ) equal to a nominal 20% of the precipitating liquid water in the given DSD sample and with an attenuation coefficient of  $0.84M \text{ dB km}^{-1}$ . We shall refer to this DSD case as  $N_{CC}$ . This case is retained only to illustrate the cloud shadow effect. Clearly, more studies would need to be undertaken to account for the variability of nonprecipitating liquid water and its effect in the uncertainty in the estimated rain rates.

To verify the accuracy of this dual-frequency Bayesian approach, it was tested on synthetic data which was constructed as follows. Starting with the rain-rate profiles obtained from the single-frequency TRMM radar algorithm over hurricane Bonnie on 22 August 1998, we superimposed the DSD model  $N_{T_0}$  with various values of the parameter  $D''$ , making sure to vary  $D''$  in all three spatial dimensions. We then (re)synthesized measured reflectivity profiles  $Z_{14}$  and  $Z_{35}$  at the TRMM resolution but assuming sensitivity thresholds of 17 dBZ at 14 GHz and 15 dBZ at 35 GHz. We then applied the Bayesian approach described above to verify that the estimates do match the original rates and the superimposed values of  $D''$ . The results are illustrated in Fig. 4, which shows estimated versus original rain rates, grouped into two seasons, one consisting of profiles where the values of  $D''$  in the superimposed DSD

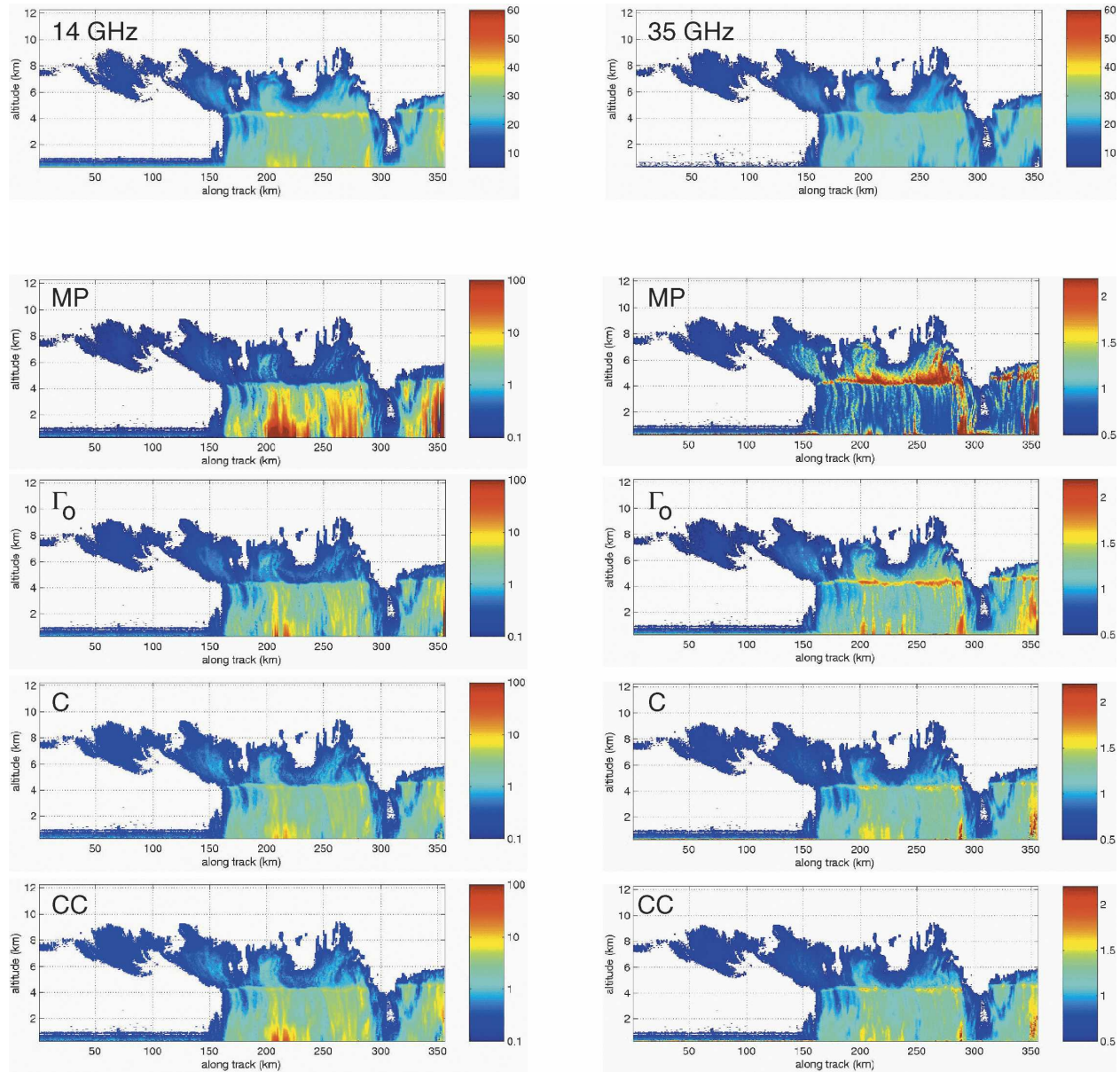


FIG. 5. (top) Tropical Storm Gabrielle—measured radar reflectivities in dB, (left) retrieved rain rates  $R$  in  $\text{mm h}^{-1}$ , and (right) mass-weighted mean drop diameters  $D^*$  in mm.

were low (the low- $D$  season) and one where the value of  $D^*$  were large (the high- $D$  season). For comparison, single-frequency (14 GHz) retrievals are also shown. The scatter in the dual-frequency Bayesian retrieval did increase substantially below 1 and above  $12 \text{ mm h}^{-1}$ , but that was expected since at low rain rates the second frequency simply adds no independent information and at high rain rates the significant 35-GHz attenuation forces the 35-GHz echo below the assumed sensitivity threshold. Thus one can conclude that the Bayesian dual-frequency approach performs quite satisfactorily.

#### 4. The CAMEX-4 results

We are now ready to apply the retrieval procedure outlined above to the data collected by JPL’s airborne PR-2 radar (Sadowy et al. 2003) over tropical storm Gabrielle and Hurricane Humberto during the CAMEX-4 experiment. Figures 5–8 show the results of the retrievals. The top two panels of Fig. 5 show the rather low radar reflectivities measured at nadir over Tropical Storm Gabrielle on 15 September 2001. The system had just emerged off the Florida coast over the

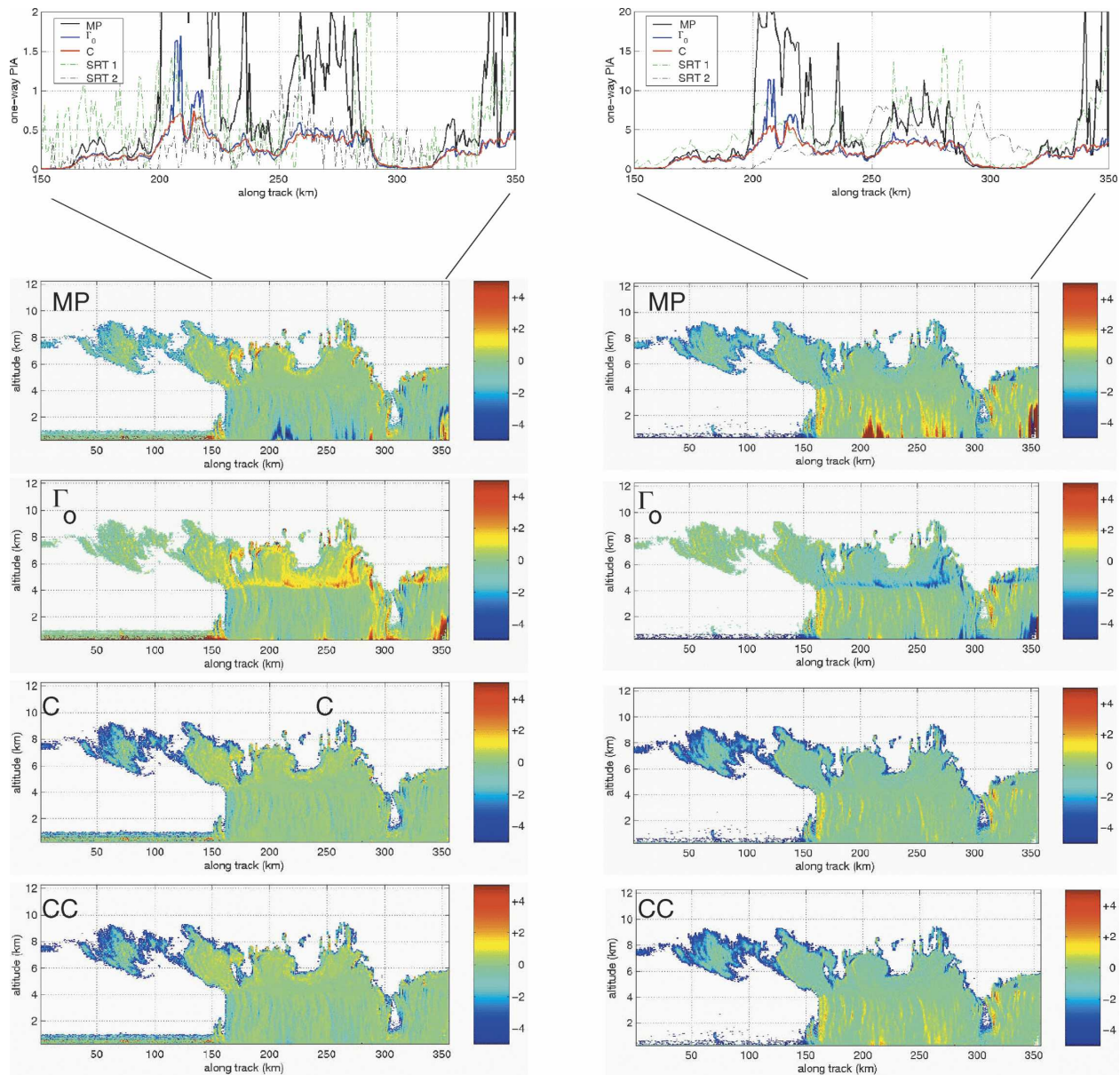


FIG. 6. Tropical Storm Gabrielle-PIA in dB [at (top left) 14 and (top right) 35 GHz; the measured attenuations according to the two surface-reference methods are shown in dashed lines, while the estimates from three of the DSD models are shown in black in the case of  $N_{MP}$ , blue in the case of  $N_{\Gamma_0}$ , and red in the case of  $N_C$ ] as well as the reflectivity errors  $Z - Z_{reconstructed}$  in dB [at (left) 14 and (right) 35 GHz].

Gulf Stream (around  $30^\circ\text{N}$ ,  $79^\circ\text{W}$ ), but had not reintensified. The remaining panels of Fig. 5 show the retrieved rain rates and mean drop diameters for each of the DSD models  $N_{MP}$ ,  $N_{\Gamma_0}$ ,  $N_C$ , and  $N_{CC}$ . The top panels of Fig. 6 show the one-way integrated attenuations corresponding to each of the models considered, along with the surface-reference PIA estimated from two models: a single average clear-air surface-cross-section reference value, and a fitted model as in Li et al. (2002). The remaining panels of Fig. 6 show the difference be-

tween the measured radar reflectivity factors and those reconstructed from the results of the Bayesian retrieval, in each of the four cases considered in this example. The top two panels of Fig. 7 show the radar reflectivities measured at nadir over Hurricane Humberto on 24 September 2001. The cyclone was embedded in a strong southwesterly flow, and anticyclonic outflow from the convective region was quite obvious. The warm core in the eye was weak, about 2 to 3 K warmer than the surrounding environment. There was a large cirrus out-

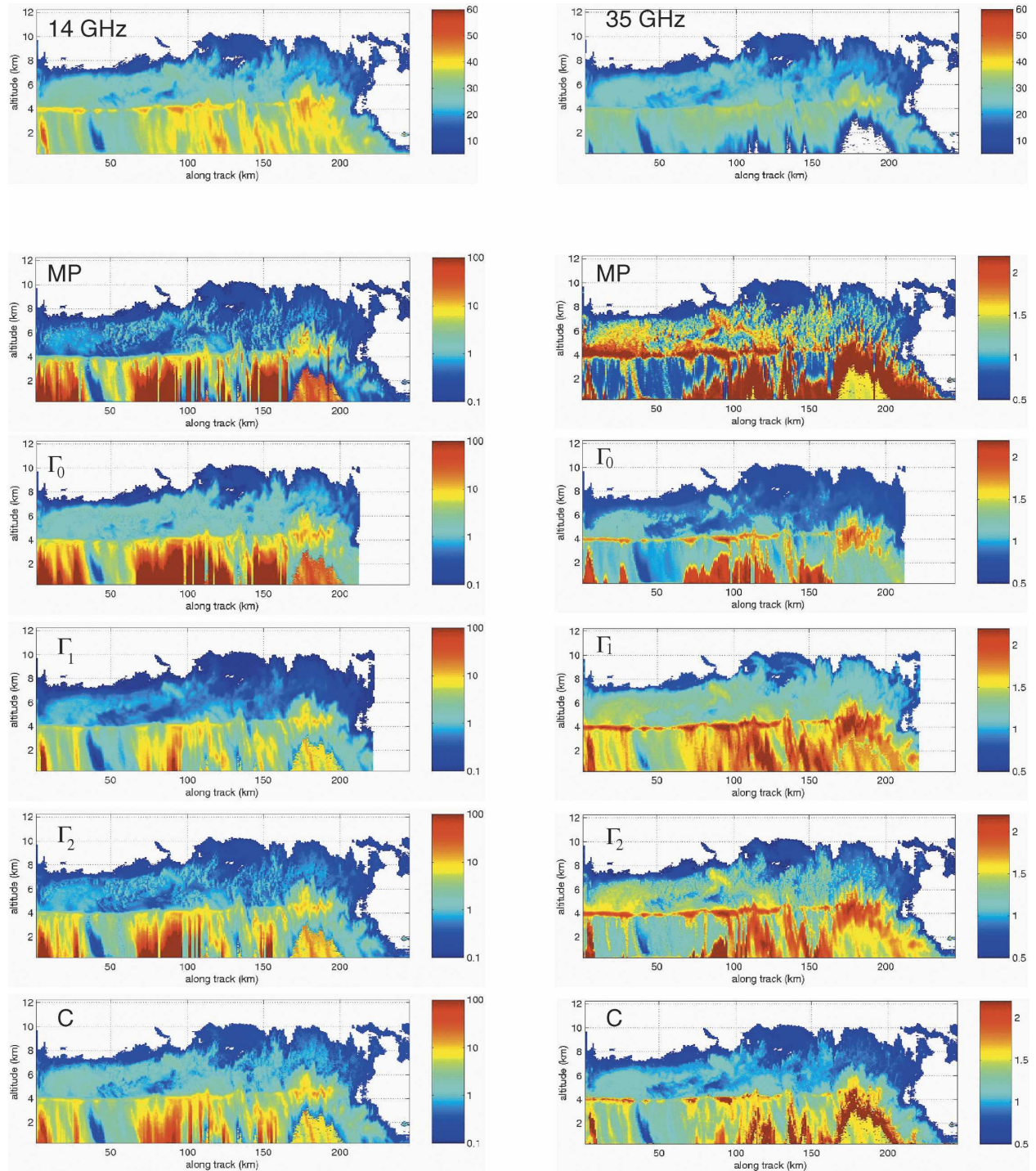


FIG. 7. (top) Hurricane Humberto—measured radar reflectivities in dB, (left) retrieved rain rates  $R$  in  $\text{mm h}^{-1}$ , and (right) mass-weighted mean drop diameters  $D^*$  in mm.

flow extending several hundred nautical miles from the center near  $37^\circ\text{N}$ ,  $63^\circ\text{W}$ . The remaining panels in Fig. 7 show the retrieved rain rates and mean drop diameters for each of the DSD models  $N_{\text{MP}}$ ,  $N_{\Gamma_0}$ ,  $N_{\Gamma_1}$ ,  $N_{\Gamma_2}$ , and  $N_C$ .

Finally, the top panels of Fig. 8 show the various PIAs, and the remaining panels of Fig. 8 show the errors in the case of  $N_{\text{MP}}$ ,  $N_{\Gamma_0}$ , and  $N_C$ .

The reflectivities measured in Gabrielle never ex-

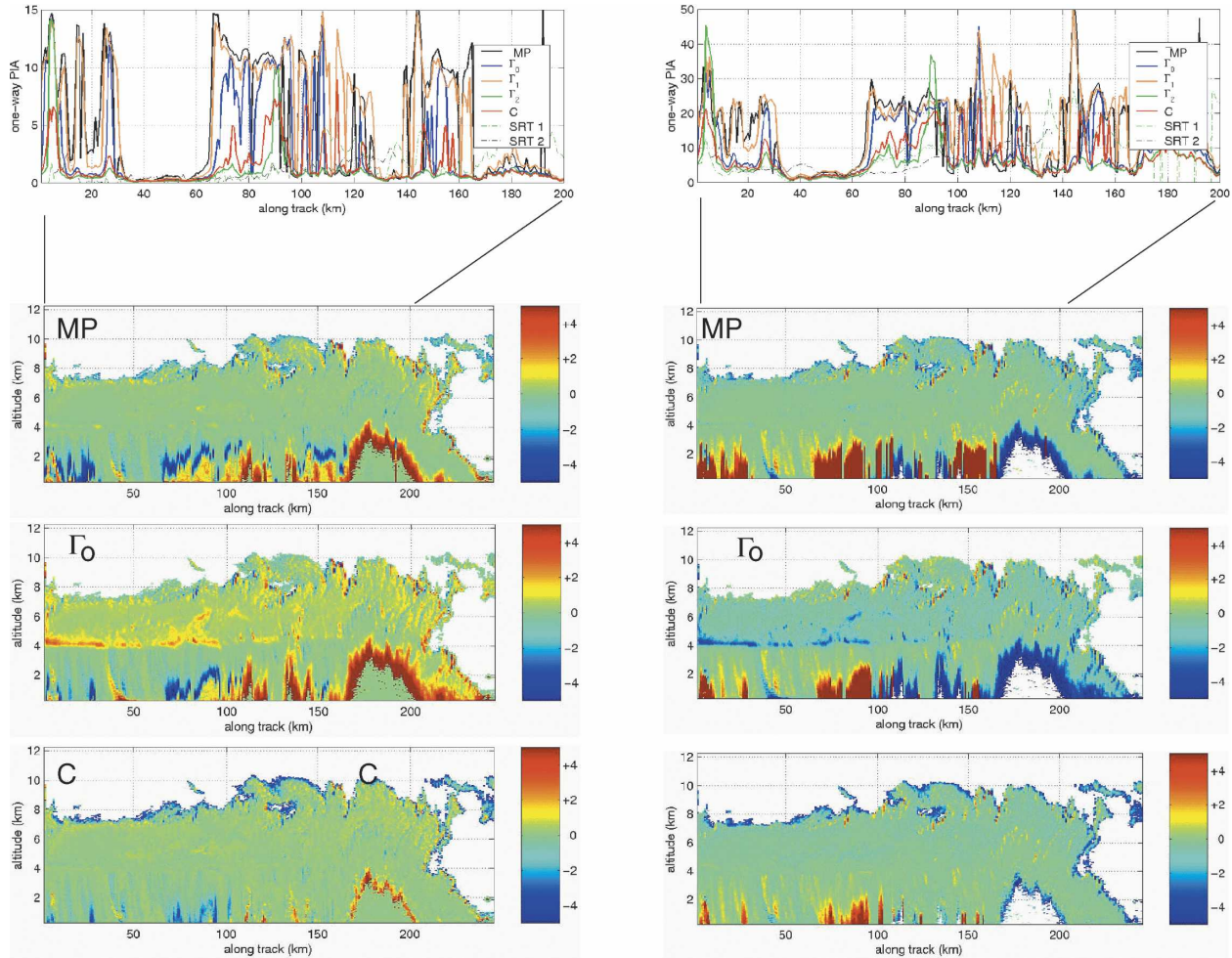


FIG. 8. Hurricane Humberto-PIA in dB [at (top left) 14 and (top right) 35 GHz, as in Fig. 6] and reflectivity errors,  $Z - Z_{\text{reconstructed}}$  in dB [at (left) 14 and (right) 35 GHz].

ceeded about 40 dBZ, and at no time was the 35-GHz echo attenuated below the sensitivity threshold of the radar. Figure 5 shows that the retrieved vertical structure of the precipitation is quite similar in all four cases considered. The exponential model MP produces unrealistically large rain rates in the three convective regions (near kilometers 220, 270, and 350), and very large mean hydrometeor sizes above the freezing level. Figure 6 confirms that the error in all four models is quite low, except within the melting layer in the restricted-gamma case  $N_{\Gamma_0}$ , where the model manifestly cannot explain the measured reflectivities without errors of about 2 dB. In general, the errors are lowest in the case of  $N_C$  and  $N_{CC}$ . A quantitative comparison of the estimates obtained using the various DSD models reveals significant differences between  $N_{MP}$  on one hand and the three other models on the other hand. Indeed, the average vertical rain-rate profile estimated

using any of the DSD models except the exponential is between 2 and 3 mm h<sup>-1</sup> (with the exponential DSD model, the average rain rate increases rapidly from about 1 mm h<sup>-1</sup> at 4 km to 11 mm h<sup>-1</sup> near the surface). Similarly, except in the exponential case, the average vertical mean-drop size profile increases from the top to a value near 1.4 mm in the melting layer, then remains near 1.2 mm from 4 km down to the surface (with the exponential DSD model, the average mean-drop size reaches 1.8 mm in the melting layer, drops to about 0.9 mm at 4-km altitude, and remains fairly constant down to the surface). As to the cloud-attenuation effect, the rain-rate estimates obtained using the rain + cloud model  $N_{CC}$  are very close to those of the rain-only model  $N_C$  aloft, though as the altitude decreases the rain rates estimated using the rain + cloud model increase steadily with respect to those of the rain-only model, the increase reaching about 50% near the sur-

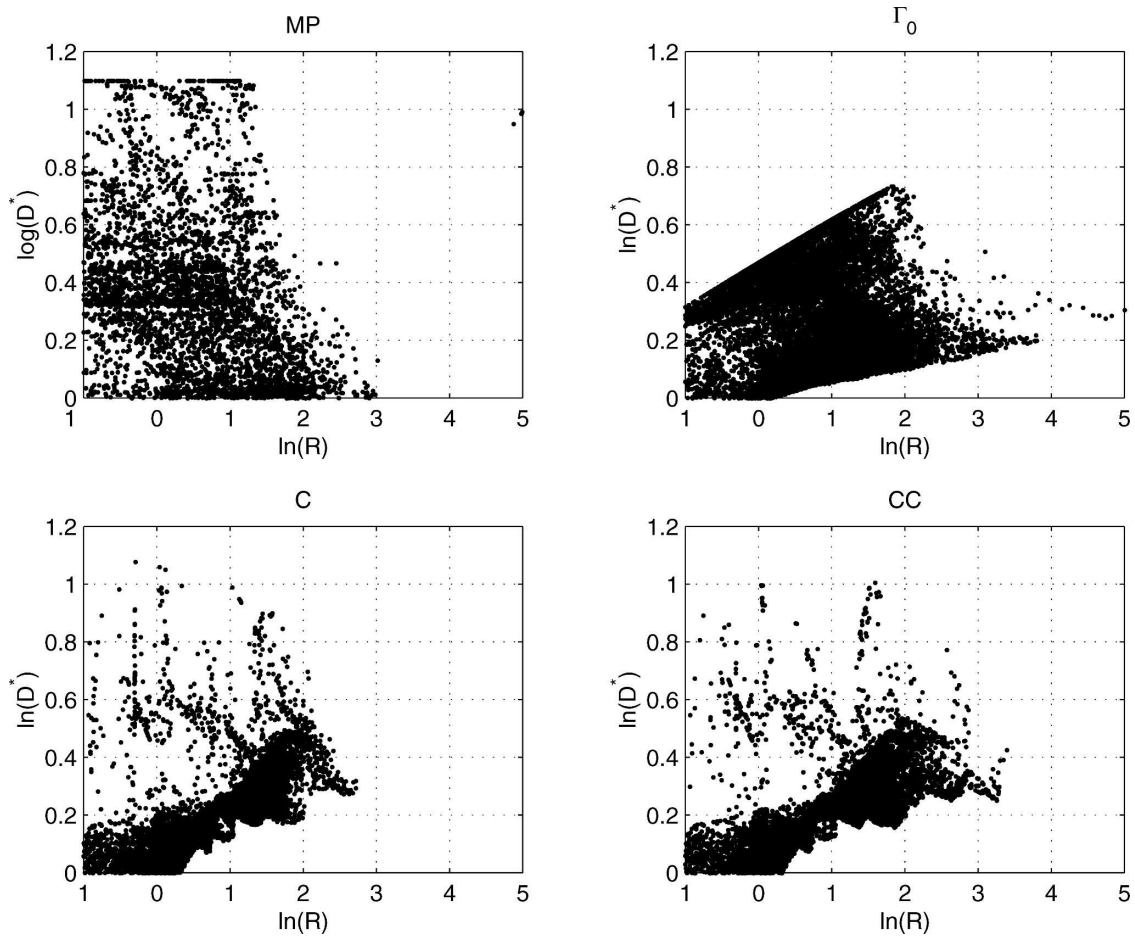


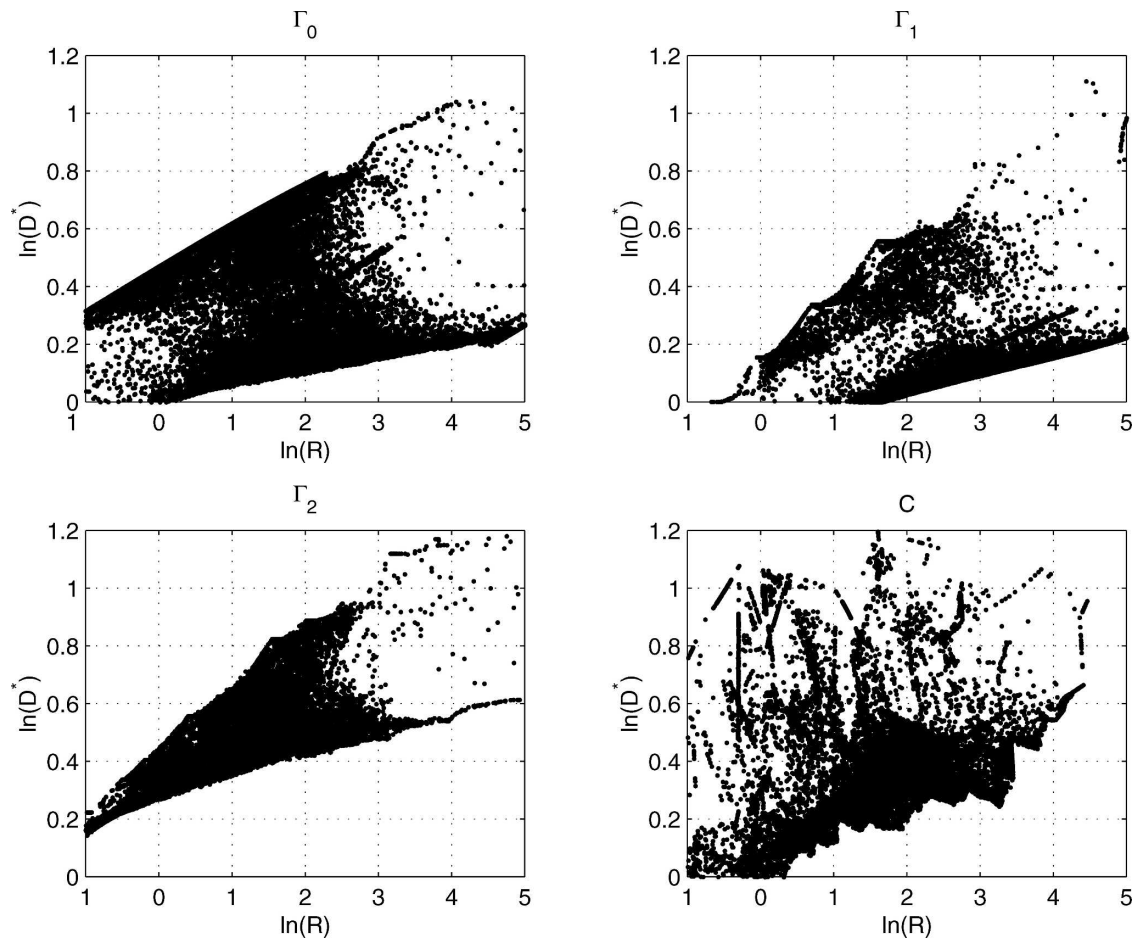
FIG. 9. Correlations between  $R$  and  $D^*$  in the case of Gabrielle.

face. However, remarkably, the mean drop size estimated by the rain + cloud and the rain-only models are almost identical.

In the case of Humberto, Fig. 7 clearly shows several cells with significant convection, and in fact the 35-GHz echo disappears at several locations along the track, most notably near kilometer 110 and between kilometers 170 and 210. The vertical structure of the retrieved rain rates and mean drop sizes from all the models except the exponential are quite similar. The latter was manifestly ill suited to explain the measurements in this case and Fig. 8 confirms that its errors are not negligible. This figure also shows that the models  $N_{\Gamma_0}$ ,  $N_{\Gamma_1}$ , and  $N_{\Gamma_2}$  (as well as  $N_{MP}$ ) fail whenever the 35-GHz is attenuated into the noise, but the raw samples model  $N_C$  produces remarkably low errors even when the 35-GHz channel is attenuated into noise. A quantitative comparison of the differences in the estimates due to the different DSD models confirms that the exponential model is the least consistent with the measurements, the database model is the most consistent, and

the restricted gamma models fall in between. Specifically, the average vertical rain rate profile in the case of  $N_{\Gamma_2}$  and  $N_C$  increases from about 4 mm h<sup>-1</sup> at 4 km to about 10.5 mm h<sup>-1</sup> near the surface; in the case of  $N_{\Gamma_0}$ , it increases from about 5 mm h<sup>-1</sup> at 4 km to rather large 40 mm h<sup>-1</sup> near the surface; and in the case of  $N_{MP}$  and  $N_{\Gamma_1}$ , it increases from about 6 mm h<sup>-1</sup> at 4 km to a rather unrealistic 90 mm h<sup>-1</sup> near the surface. As to the average mean drop size, the estimates obtained using  $N_{\Gamma_0}$  and  $N_C$  are very close, remaining near 1.5 mm from 3.5 km down to the surface; the mean drop size in the case of  $N_{\Gamma_2}$  remains near 1.7 mm from the melting layer down to the surface; and the mean drop size in the case of  $N_{\Gamma_1}$  is systematically the lowest, increasing from 1.2 mm just below the melting layer to 1.5 mm near the surface.

Most interesting, all the DSD models (except the exponential) produce rain-rate and mean-drop size estimates that are very significantly correlated. This is illustrated in Figs. 9 and 10. In the three restricted-gamma models, the joint behavior of the mean drop

FIG. 10. Correlations between  $R$  and  $D^*$  in the case of Humberto.

size and the rain rate is approximately bimodal, clustering around the upper and lower log-linear  $D^*$ - $R$  relations given in Table 1. In the database case, the estimates cluster around the piecewise log-linear relation

$$D^* = 0.95R^{0.2} \quad \text{if } R < 7.4 \quad (13)$$

$$= 1.22R^{0.075} \quad \text{if } R > 7.4. \quad (14)$$

The particularly striking fact is that for heavier rain ( $R$  greater than about  $10 \text{ mm h}^{-1}$ ), the estimates overwhelmingly cluster around the low- $D^*$  correlation curves, in all four cases. This would imply that the mean drop size at high rain rates is smaller than one would anticipate from correlation models derived from more moderate precipitation. Similarly, for lighter rain, while there is no pronounced trend in the restricted-gamma models, the estimates produced by the COARE database DSD model do cluster around a  $\log(D^*)$ - $\log(R)$  curve with a steeper slope than the one obtained at higher rain rates, implying that the mean drop size decreases more rapidly with decreasing rain rate when the

latter falls below about  $4.5 \text{ mm h}^{-1}$ . This supports the likelihood that the mean drop size at lighter precipitation is indeed smaller than one might anticipate from a correlation model derived from more intense precipitation.

## 5. Conclusions

The main conclusion of this analysis is that several quite different DSD models do indeed produce plausible dual-frequency precipitation estimates, at least over tropical systems like those observed during

TABLE 1. Retrieved  $D^*$ - $R$  relations with  $R$  in  $\text{mm h}^{-1}$  and  $D^*$  in mm.

DSD model	High- $D^*$ relation	Low- $D^*$ relation
$\Gamma_0$	$D^* = 1.42R^{0.15}$	$D^* = R^{0.044}$
$\Gamma_1$	$D^* = 1.1R^{0.17}$	$D^* = 0.91R^{0.06}$
$\Gamma_2$	$D^* = 1.45R^{0.19}$	$D^* = 1.31R^{0.066}$

CAMEX-4. The general shape of the vertical variation of the retrieved rain rates and mean drop sizes will be similar among the different models, but the precipitation amounts and the actual profiles of mean drop diameter differ from model to model, as do the resulting correlation patterns between rain rate and mean drop diameter. The most important implication is that the decision about which drop size distributions should be considered a priori plausible does have a determining effect on the eventual retrievals. It is therefore very important to justify such a priori assumptions with detailed DSD measurements at radar-sized resolutions.

*Acknowledgments.* This work was performed at the Jet Propulsion Laboratory, California Institute of Technology, under contract with the National Aeronautics and Space Administration.

#### REFERENCES

- Eccles, P. J., and E. A. Mueller, 1971: X-band attenuation and liquid water content estimation by dual-wavelength radar. *J. Appl. Meteor.*, **10**, 1252–1259.
- Fujita, M., 1983: An algorithm for estimating rain rate by a dual-frequency radar. *Radio Sci.*, **18**, 697–708.
- Haddad, Z. S., A. R. Jameson, E. Im, and S. L. Durden, 1995: Improved coupled  $Z$ - $R$  and  $k$ - $R$  relations and the resulting ambiguities in the determination of the vertical distribution of rain from the radar backscatter and the integrated attenuation. *J. Appl. Meteor.*, **34**, 2680–2688.
- , D. A. Short, S. L. Durden, E. Im, S. Hensley, M. B. Grable, and R. A. Black, 1997a: A new parametrization of the raindrop size distribution. *IEEE Trans. Geosci. Remote Sens.*, **35**, 532–539.
- , E. A. Smith, C. D. Kummerow, T. Iguchi, M. R. Farrar, S. L. Durden, M. Alves, and W. S. Olson, 1997b: The TRMM ‘Day-1’ radar/radiometer combined rain-profiling algorithm. *J. Meteor. Soc. Japan*, **75**, 799–809.
- Iguchi, T., T. Kozu, R. Meneghini, J. Awaka, and K. Okamoto, 2000: Rain-profiling algorithm for the TRMM precipitation radar. *J. Appl. Meteor.*, **39**, 2038–2052.
- Li, L., E. Im, S. L. Durden, and Z. S. Haddad, 2002: A surface wind model-based method to estimate rain-induced radar path attenuation over ocean. *J. Atmos. Oceanic Technol.*, **19**, 658–672.
- Lukas, R., P. J. Webster, M. Ji, and A. Leetmaa, 1995: The large-scale context of the TOGA Coupled Ocean Atmosphere Response Experiment. *Meteor. Atmos. Phys.*, **56**, 3–16.
- Marshall, J. S., and W. M. K. Palmer, 1948: The distribution of raindrops with size. *J. Meteor.*, **5**, 165–166.
- Marzoug, M., and P. Amayenc, 1994: A class of single- and dual-frequency algorithms for rain-rate profiling from a spaceborne radar. Part I: Principle and tests from numerical simulations. *J. Atmos. Oceanic Technol.*, **11**, 1480–1506.
- Meagher, J. P., and Z. S. Haddad, 2002: Principal-component analysis for raindrops and its application to the remote sensing of rain. *Quart. J. Roy. Meteor. Soc.*, **128**, 559–571.
- Meneghini, R., and K. Nakamura, 1990: Range profiling of the rain rate by an airborne weather radar. *Remote Sens. Environ.*, **31**, 193–209.
- Sadowy, G. A., A. C. Berkun, W. Chun, E. Im, and S. L. Durden, 2003: Development of an advanced airborne precipitation radar. *Microwave J.*, **46**, 84–98.
- Smith, E. A., and A. Mugnai, 1988: Radiative transfer to space through a precipitating cloud at multiple microwave frequencies. Part II: Results and analysis. *J. Appl. Meteor.*, **27**, 1074–1091.
- Ulbrich, C. W., 1983: Natural variations in the analytical form of the raindrop size distribution. *J. Climate Appl. Meteor.*, **22**, 1764–1775.
- , and D. Atlas, 1998: Rainfall microphysics and radar properties: Analysis methods for drop size spectra. *J. Appl. Meteor.*, **37**, 912–923.